

## 3D ISOTROPIC ELASTIC REVERSE TIME MIGRATION USING SIGNED MAGNITUDES OF ELASTIC DATA COMPONENTS

WENLONG WANG<sup>1</sup> and GEORGE A. MCMECHAN<sup>2</sup>

<sup>1</sup> Department of Mathematics, Harbin Institute of Technology, 92 Xidazhi St., Nangang Dist., Harbin, Heilongjiang 150001, P.R. China. wenlong.wang@hit.edu.cn

<sup>2</sup> Center for Lithospheric Studies, The University of Texas at Dallas, 800 W. Campbell Road, Richardson, TX 75080-3021, U.S.A. mcmec@utdallas.edu

(Received July 29, 2018; accepted April 15, 2019)

### ABSTRACT

Wang, W. and McMechan, G.A., 2019. 3D isotropic elastic reverse time migration using signed magnitudes of elastic data components. *Journal of Seismic Exploration*, 28: 221-244.

Elastic reverse time migration (ERTM) is capable of characterizing subsurface properties more completely than its acoustic counterpart. P- and S-waves coexist in elastic wavefields, and their separation is required before, or as part of, applying the image conditions. Traditional P- and S-wave separation methods based on divergence and curl operators don't preserve the elastic vector information, and the associated polarity reversals of S-wave images are difficult to handle. Thus a preferable workflow for isotropic ERTM should include a vector decomposition of the elastic wavefields and a vector-based image condition that directly uses the signed magnitudes of the decomposed vector wavefields to produce PP and PS images. We propose a new 3D elastic image condition which is a source-normalized crosscorrelation of the signed magnitudes of the decomposed wavefields. The image condition is robust and stable for generating 3D PP and PS images and their corresponding angle domain common-image gathers (ADCIGs) with incident angles calculated from Poynting vectors. Comparisons between the proposed image condition and a vector-based dot-product image condition and show that the proposed image condition generates PP ADCIGs with a wider range of incident angles than existing dot-product image conditions.

KEY WORDS: 3D, RTM, elastic, image condition.

## INTRODUCTION

Elastodynamic wave equations can simulate seismic wave propagation with fewer assumptions than acoustic wave equations, as the former include both shear- and compressional wave propagations. 3D elastic migration, with multicomponent data as input, provides the foundation for structure imaging and elastic parameter estimation.

Migration of multicomponent data has been attempted in the past, using either ray-based or wave-based solutions. Ray-based examples include Kirchhoff migration (Kuo and Dai, 1984; Dai and Kuo, 1986; Hokstad, 2000), where PP- and PS-wave traveltimes are calculated and amplitudes are summed along their corresponding traveltime trajectories. The PS separation is done implicitly by using P- and S-velocity models to compute the corresponding traveltimes. Multicomponent elastic Kirchhoff migration has the same limitations as acoustic Kirchhoff migrations; wave phenomena cannot be fully described by ray theory if the geology becomes complicated (Gray et al., 2001). Wave-based solutions (Chang and McMechan, 1986, 1994; Whitmore, 1995), on the other hand, reconstruct the wavefields with a wave equation (Wapenaar and Haimé, 1990), and have fewer limitations than ray-based migrations. Sun and McMechan (2001) separate multicomponent data near the surface and use acoustic equations for separate PP and PS migrations. Elastic reverse time migration (ERTM) utilizes elastic wave equations directly, and constructs the source elastic wavefields forward in time and reconstructs the receiver elastic wavefields backward in time by using multicomponent seismic data as initial, and boundary conditions, respectively.

Different image conditions are applied in ERTMs. Early attempts include the excitation time image condition (Chang and McMechan, 1986), in which the image time is calculated by raytracing from the source point. The crosscorrelation image condition (Claerbout, 1985) remains the standard image condition for acoustic RTMs, but in ERTMs, a component-by-component crosscorrelation causes crosstalk between the unseparated P- and S-waves leads to artifacts which pose difficulties in interpretation. Yan and Sava (2008) apply divergence and curl operators to separate the P- and S-waves before applying the crosscorrelation image condition and demonstrate improvements in image quality. The polarity reversal problem of the PS image is generated by the curl operators and needs special treatment/corrections (Du et al., 2012, 2014) to avoid destructive interference in post-migration stacking. This phase shift does not occur in the proposed algorithm. Rocha et al. (2016) propose an energy norm image condition for elastic imaging which constructs a single image from all wave modes, thus no wave mode separation or decompositions are

needed. However, the P- and S-waves have distinctive properties during propagation in different media, and generating PP and PS images separately is helpful for interpretation purposes, for example the detection of fluids (Stewart, 1990).

Recently, P- and S-wave vector decomposition (Ma and Zhu, 2003; Zhang et al., 2007; Wang et al., 2015, 2016b; Zhu, 2017; Wang et al., 2018) is gaining popularity. Vector decomposition preserves the amplitude and phase in the input elastic wavefield and retains the same physical magnitude and units, and thus is considered to be more accurate than using divergence and curl operators which change the phase and amplitude of the input wavefield.

Wang et al. (2016) and Du et al. (2017) obtain decomposed elastic vectors from a source and receiver wavefield and use a dot product type of crosscorrelation image condition to generate images. The dot product, however, leads to image amplitude changes as a function of the open angle between the incident and reflected (converted) waves, causing difficulties in AVA analysis. Du et al. (2017) also propose to crosscorrelate P-wave stresses as an alternative to construct PP images. Wang and McMechan (2015, 2016) use the signed magnitude ratio to construct images by a 2D (or 3D) excitation amplitude image condition. This image condition applies Poynting vectors (Červený, 2001) calculated from decomposed P- and S-waves to obtain angle-domain common-image gathers (ADCIGs). The excitation amplitude image condition (Nguyen and McMechan, 2013; Wang and McMechan, 2015) features a significant reduction in the source wavefield storage and the I/O burden, but it requires sophisticated improvements to include multipathing (Jin et al., 2015), which is common in complicated models. In this paper, we extend the previous excitation amplitude based elastic image condition to a more robust source-normalized magnitude-crosscorrelation type image condition and apply it to 3D ERTMs.

P- and S-wave vector decomposition is also possible in anisotropic wavefields (Cheng and Fomel, 2014; Wang et al., 2018). However, we limit the scope of this initial elastic paper to isotropic media, as a main goal is the proof of concept. The paper is organized as follows; first the methodology for obtaining decomposed P- and S-wave vectors is described. Then we illustrate the procedure for implementing the 3D source-normalized magnitude-crosscorrelation elastic image condition. To limit the scope, only PP and PS images are generated and analyzed in this paper. The proposed 3D ERTM procedure is successfully tested on a single-layer model and a portion of the SEG/EAGE Overthrust model (Aminzadeh et al., 1994).

## METHODOLOGY

The procedure of 3D source-normalized magnitude-crosscorrelation ERTM is similar to that of the 2D excitation amplitude ERTM image condition Wang and McMechan (2015). In ERTMs, the source wavefield is extrapolated before the receiver wavefield extrapolation. Both elastic wavefield extrapolations involve P- and S-wavefield decompositions. The decomposed P- and S-wave particle-velocities and stresses are used to obtain their propagation directions and reflection polarities. In the following subsections, the procedures are explained and illustrated in detail.

### 3D elastic wavefield extrapolation and PS decomposition

We use the 3D stress-particle-velocity formulation proposed by Madariaga (1976) and Virieux (1984), which includes the general Hooke's law

$$\frac{\partial \tau_{xx}}{\partial t} = (\lambda + 2\mu) \left( \frac{\partial v_x}{\partial x} + \frac{\partial v_y}{\partial y} + \frac{\partial v_z}{\partial z} \right) - 2\mu \left( \frac{\partial v_y}{\partial y} + \frac{\partial v_z}{\partial z} \right), \quad (1a)$$

$$\frac{\partial \tau_{yy}}{\partial t} = (\lambda + 2\mu) \left( \frac{\partial v_x}{\partial x} + \frac{\partial v_y}{\partial y} + \frac{\partial v_z}{\partial z} \right) - 2\mu \left( \frac{\partial v_x}{\partial x} + \frac{\partial v_z}{\partial z} \right), \quad (1b)$$

$$\frac{\partial \tau_{zz}}{\partial t} = (\lambda + 2\mu) \left( \frac{\partial v_x}{\partial x} + \frac{\partial v_y}{\partial y} + \frac{\partial v_z}{\partial z} \right) - 2\mu \left( \frac{\partial v_x}{\partial x} + \frac{\partial v_y}{\partial y} \right), \quad (1c)$$

$$\frac{\partial \tau_{xy}}{\partial t} = \mu \left( \frac{\partial v_x}{\partial y} + \frac{\partial v_y}{\partial x} \right), \quad (1d)$$

$$\frac{\partial \tau_{xz}}{\partial t} = \mu \left( \frac{\partial v_x}{\partial z} + \frac{\partial v_z}{\partial x} \right), \quad (1e)$$

$$\frac{\partial \tau_{yz}}{\partial t} = \mu \left( \frac{\partial v_y}{\partial z} + \frac{\partial v_z}{\partial y} \right), \quad (1f)$$

and the equations of motion

$$\rho \frac{\partial v_x}{\partial t} = \frac{\partial \tau_{xx}}{\partial x} + \frac{\partial \tau_{xy}}{\partial y} + \frac{\partial \tau_{xz}}{\partial z}, \quad (2a)$$

$$\rho \frac{\partial v_y}{\partial t} = \frac{\partial \tau_{xy}}{\partial x} + \frac{\partial \tau_{yy}}{\partial y} + \frac{\partial \tau_{yz}}{\partial z}, \quad (2b)$$

$$\rho \frac{\partial v_z}{\partial t} = \frac{\partial \tau_{xz}}{\partial x} + \frac{\partial \tau_{yz}}{\partial y} + \frac{\partial \tau_{zz}}{\partial z}, \quad (2c)$$

where  $\tau$  is stress and  $v$  is particle-velocity, and the subscripts indicate x-, y- or z-coordinates.

The stress-particle-velocity formulation extrapolates 3D isotropic elastic wavefields with coupled P- and S-waves; if they are not separated either before extrapolation, or as part of the image condition, they will be

superimposed as 'crosstalk' artifacts in the migrated images. Instead of using divergence and curl operators, which produce scalar and vector pseudo-potentials rather than particle vector components (Aki and Richards, 1980; Yan and Sava, 2008), we decompose the wavefields while preserving their vector amplitude and phase. This can be achieved by calculating an auxiliary P-wave stress  $\tau_p$  which is a scalar wavefield similar to pressure in the acoustic wave equation, while solving the complete stress-particle-velocity formulation in eqs. (1) and (2). The calculation for P-wave stress has a scalar form (Xiao and Leaney, 2010)

$$\frac{\partial \tau_p}{\partial y} = (\lambda + 2\mu) \left( \frac{\partial v_x}{\partial x} + \frac{\partial v_y}{\partial y} + \frac{\partial v_z}{\partial z} \right). \quad (3)$$

Then the horizontal and vertical particle-velocity components of P-waves,

$v_x^p$ ,  $v_y^p$  and  $v_z^p$ , are calculated from  $\tau_p$  by finite differencing

$$\frac{\partial v_x^p}{\partial t} = \frac{1}{\rho} \frac{\partial \tau_p}{\partial x}, \quad (4a)$$

$$\frac{\partial v_y^p}{\partial t} = \frac{1}{\rho} \frac{\partial \tau_p}{\partial y}, \quad (4b)$$

and

$$\frac{\partial v_z^p}{\partial t} = \frac{1}{\rho} \frac{\partial \tau_p}{\partial z}. \quad (4c)$$

This gives a complete description of the vector P-wavefield; the S-wavefield can be obtained by subtracting the P-wavefield from the complete wavefield, component-by-component

$$v_x^s = v_x - v_x^p, \quad (5a)$$

$$v_y^s = v_y - v_y^p, \quad (5b)$$

and

$$v_z^s = v_z - v_z^p. \quad (5c)$$

where  $v_x^s$ ,  $v_y^s$  and  $v_z^s$  are the x-, y- and z-direction particle-velocity components of the S-waves.

An example of elastic wavefield decomposition is shown in Fig. 1,

where an explosive source and a rotational source in the x-z plane are placed at the center of a homogeneous model with propagation velocities  $V_P = 2.5$  km/s,  $V_S = 1.6$  km/s, and  $\rho = 2.1$  kg/cm<sup>3</sup>. The first row (Figs. 1a - 1c) are the x-, y- and z-components of the original elastic wavefield snapshot; the second (Figs. 1d - 1f) and the third (Figs. 1g - 1i) rows are the corresponding decomposed components of the P- and the S-waves with vector components preserved.

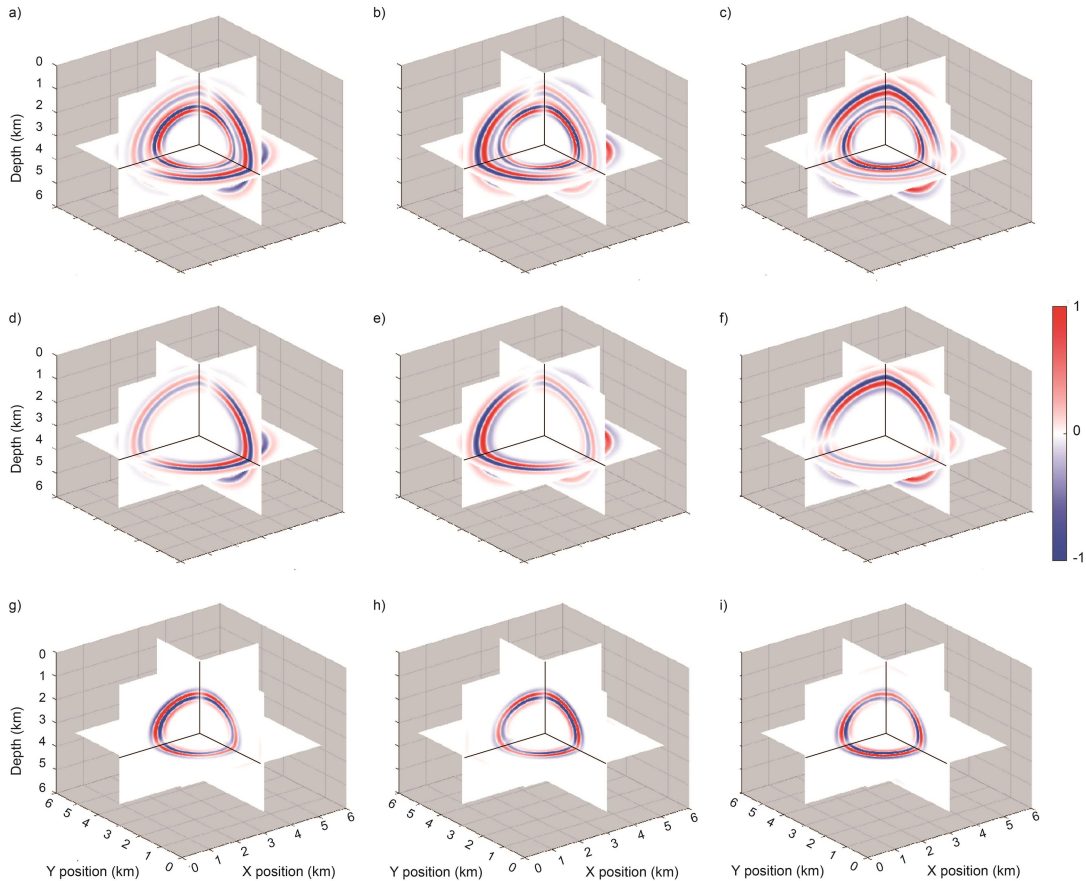


Fig. 1. An elastic wavefield decomposition example in a homogeneous model. (a)-(c) are the X-, Y- and Z-components of the original particle-velocity components; (d)-(f) are the X-, Y- and Z-components of the decomposed P-wave particle-velocity components; (g)-(i) are the X-, Y- and Z-components of the decomposed S-wave particle-velocity components.

### 3D source-normalized magnitude-crosscorrelation ERTM image condition

During the source wavefield extrapolation, the decomposed P-wavefield needs to be stored as time series snapshots, which includes the

particle-velocities ( $v_{(src)x}^p, v_{(src)y}^p, v_{(src)z}^p$ ) and the P-wave stress  $\tau_p$ . The vector magnitudes of the particle-velocities of the source and receiver wavefields are crosscorrelated in the image condition, and both particle-velocities and stresses of each wavefield are input to obtain Poynting vectors (Červený, 2001).

$$s_j^p = -\tau_p v_j^p, \quad (6)$$

where  $s_j^p$  are the P-wave Poynting vector components, and  $v_j^p$  are the components of the decomposed P-wave particle-velocity, for  $j = x, y, z$ . In this paper, we are interested in the PP and PS images, in which the incident wavefields are P-waves only; thus the S-wave Poynting vectors are not required to be calculated, although this has been done by Wang et al. (2016b).

The reverse-time receiver extrapolation follows the source extrapolation, during which the image condition is applied. We use the signed-magnitude crosscorrelation to construct the image. During application of the image condition, the signs of the reflections (of both PP and PS) are calculated as a function of position, incident angle and azimuth angle.

The signs of both PP and PS reflections can be determined from the principle that the incident and the reflected waves have the same polarity for a negative reflection coefficient, and opposite polarity for a positive reflection coefficient (Aki and Richards, 1980). For 3D models, the calculation for the signs of the reflections is more complicated. We assume only P-waves are present in the source wavefield, so theoretically, the reflections are all either PP or PSV, and the particle-velocity directions, propagation directions, and reflector normal are all in the same plane, for a reflection at a grid point. The azimuth angle is obtained from

$$\phi = \text{atan2}[s_{(src)y}^p, s_{(src)x}^p] , \quad (7)$$

where  $s_{(src)x}^p$  and  $s_{(src)y}^p$  are the x- and y-components of the P-wave Poynting vectors [eq. (6)] calculated from the source wavefield at each grid point and image time. For PP reflections, the incident and reflection angles are the same in an isotropic medium. The incident angle  $\theta$  can then be solved from the vector dot product geometrical relation (Du et al., 2017; Shabelansky, 2017; Zhu, 2017) as

$$\tilde{\mathbf{S}}_{src}^p \cdot \tilde{\mathbf{S}}_{rec}^p = |\tilde{\mathbf{S}}_{src}^p| |\tilde{\mathbf{S}}_{rec}^p| \cos(2\theta), \quad (8)$$

where the  $\tilde{\mathbf{S}}_{src}^p$  and  $\tilde{\mathbf{S}}_{rec}^p$  are the normalized decomposed P-wave Poynting vectors of the source and the receiver wavefields, respectively. During the normalization, a threshold is applied to the magnitudes of the Poynting vectors, which are used as denominators for normalization, to prevent division by zero. This scheme is applied to both elastic image conditions which are compared in the Synthetic Tests section.  $|\cdot|$  represents the magnitude of the vector argument. As proposed by Du et al. (2014), the reflector normal direction  $\vec{n}$  can be obtained from

$$\vec{n} = \tilde{\mathbf{S}}_{src}^p - \tilde{\mathbf{S}}_{rec}^p. \quad (9)$$

Similarly, the reflector dip direction  $\vec{d}$  can be calculated from

$$\vec{d} = \tilde{\mathbf{S}}_{src}^p + \tilde{\mathbf{S}}_{rec}^p. \quad (10)$$

To stabilize the Poynting vectors in complex wavefields, we apply a median filter to the calculated propagation directions in the space domain (Jin et al., 2014).

The polarity of a PP reflection can be observed through its particle

motion normal to the reflector (Fig. 2a). To determine if the polarity of the PP reflection changes at a grid point, the recorded source P-wave particle-velocity vector  $\mathbf{V}_{src}^p$  can be projected to the reflector normal direction  $\vec{n}$ , to give the projected vector  $\hat{\mathbf{V}}_{src}^p$ . Then the decomposed P-wave particle-velocity components of the receiver wavefield  $\mathbf{V}_{rec}^p$  can also be projected to the reflector normal direction  $\vec{n}$  to give  $\hat{\mathbf{V}}_{rec}^p$ . The sign of PP reflection at each grid point can be obtained from

$$\text{sgn}_{pp}(x, y, z, t, \theta, \phi) = \begin{cases} +1, & \text{if } \hat{\mathbf{V}}_{src}^p(x, y, z, t) \cdot \hat{\mathbf{V}}_{rec}^p(x, y, z, t) < 0, \\ -1, & \text{if } \hat{\mathbf{V}}_{src}^p(x, y, z, t) \cdot \hat{\mathbf{V}}_{rec}^p(x, y, z, t) > 0. \end{cases} \quad (11)$$

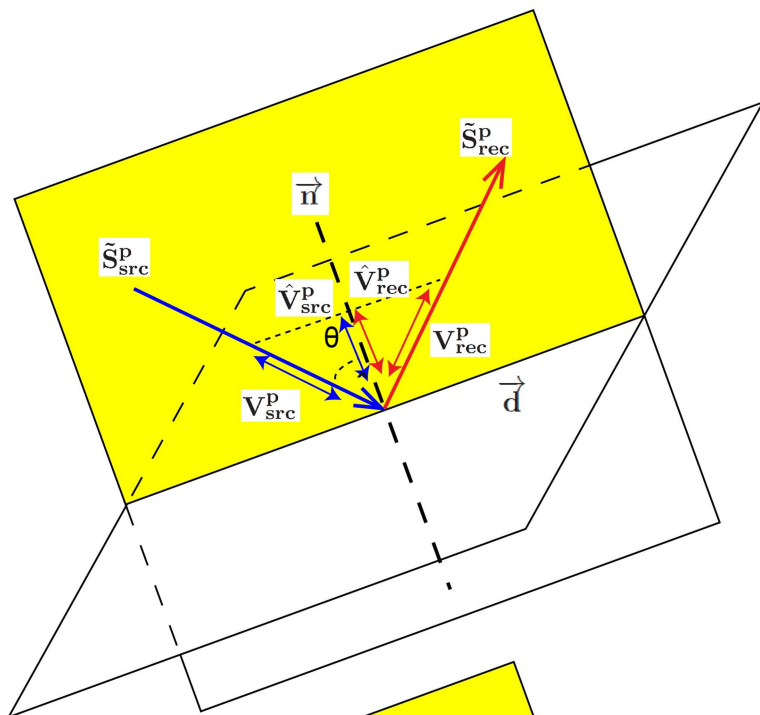
where the  $\theta$  and  $\phi$  are incident and azimuth angles calculated from the Poynting vectors as discussed above.

The polarity change of a PS reflection is determined from its particle motion parallel to the reflector (Fig. 2b) (Aki and Richards, 1980). Similar to the procedure to get PP reflection signs, we project the recorded source P-wave particle-velocity components  $\mathbf{V}_{src}^p$  and the receiver S-wave particle-velocity components  $\mathbf{V}_{rec}^s$  on the reflector  $\mathbf{r}$  to get their projections  $\check{\mathbf{V}}_{src}^p$  and  $\check{\mathbf{V}}_{rec}^s$ , and the sign of the PS reflection can be obtained using

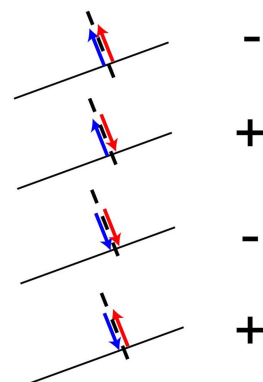
$$\text{sgn}_{ps}(x, y, z, t, \theta, \phi) = \begin{cases} +1, & \text{if } \check{\mathbf{V}}_{src}^p(x, y, z, t) \cdot \check{\mathbf{V}}_{rec}^s(x, y, z, t) < 0, \\ -1, & \text{if } \check{\mathbf{V}}_{src}^p(x, y, z, t) \cdot \check{\mathbf{V}}_{rec}^s(x, y, z, t) > 0. \end{cases} \quad (12)$$

This is different from the polarity correction strategy proposed by Du et al. (2012, 2014), in which the polarity reversal problem is brought by the curl operators, while in our approach, the elastic components are preserved after decomposition, as no curl operators are involved, and the polarity doesn't need to be corrected. Eq. (12) is designed to find the sign of PS reflection coefficients from the relations between the polarizations and their propagation directions.

a)



Particle velocity projections Sign



b)

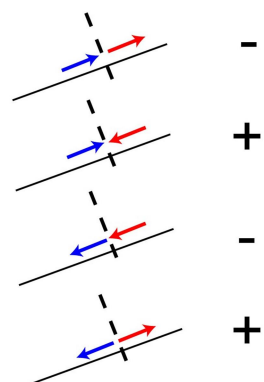
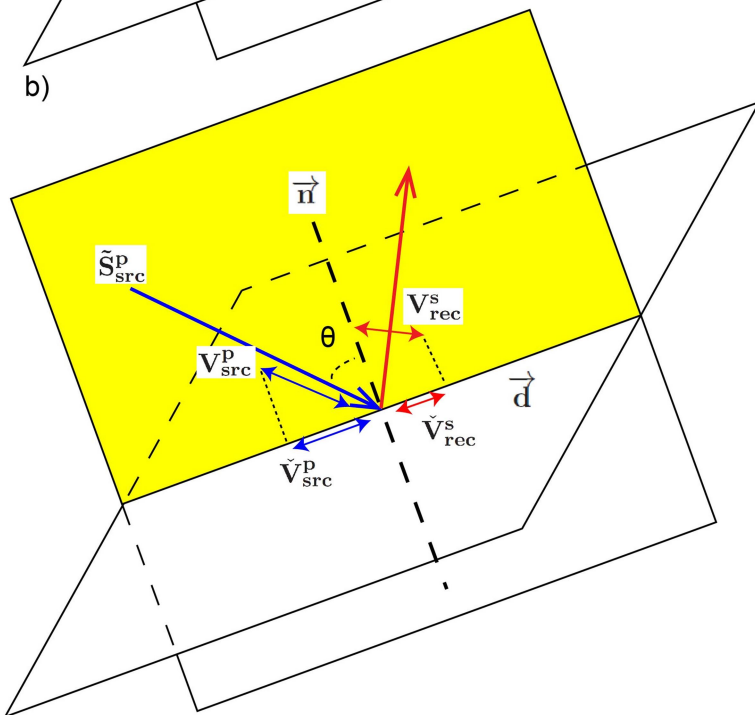


Fig. 2. Kinematic example of (a) PP and (b) PS reflection particle-velocities and corresponding polarities (3D).

With knowledge of the signs of a PP or a PS reflection, we use the magnitude of the receiver (reflected) P- or S-waves crosscorrelated with the source (incident) magnitude to obtain an image, and then it is source normalized to represent the reflectivity (Sheriff and Geldart, 1995) at each image point.

$$I_{pp}(x, y, z) = \frac{\sum_{t=0}^T \text{sgn}_{pp}(x, y, z, t) |\mathbf{V}_{rec}^p(x, y, z, t)| |\mathbf{V}_{src}^p(x, y, z, t)|}{\sum_{t=0}^T |\mathbf{V}_{src}^p(x, y, z, t)|^2}, \quad (13)$$

$$I_{ps}(x, y, z) = \frac{\sum_{t=0}^T \text{sgn}_{ps}(x, y, z, t) |\mathbf{V}_{rec}^s(x, y, z, t)| |\mathbf{V}_{src}^p(x, y, z, t)|}{\sum_{t=0}^T |\mathbf{V}_{src}^p(x, y, z, t)|^2},$$

where  $I_{pp}$  and  $I_{ps}$  are PP and PS images. The incident angle  $\theta$  and azimuth angle  $\phi$  are hidden for simplicity, but need to be included in the evaluation of eq. (13).

The differences and relations between the proposed image condition and the dot product image condition (Wang et al., 2016a; Du et al., 2017) can be found in Appendix A.

## SYNTHETIC TESTS

The proposed image condition is first tested on a flat layered elastic model (Fig. 3). The upper layer has  $V_p = 2.5$  km/s,  $V_s = 1.6$  km/s and  $\rho = 2.1$  g/cm<sup>3</sup>; the lower layer has  $V_p = 2.8$  km/s,  $V_s = 1.7$  km/s and  $\rho = 2.2$  g/cm<sup>3</sup>. The wavefields are extrapolated with an eighth-order in space, second-order in time, stress-particle-velocity, staggered-grid, finite-difference solution [eqs. (1) and (2)]. Convolutional perfectly matched layer (CPML) absorbing boundary conditions (Komatitsch and Martin, 2007) are used on all six grid edges to reduce unwanted reflections. The model (Fig. 3) has 5 m grid spacing in the x- y- and z-directions. Eight explosive sources with a 15 Hz Ricker wavelet are initiated and migrated one after another. The sources are evenly spaced on the surface along a circle with the center at  $(x, y) = (0.25, 0.25)$  km and radius = 0.02 km;  $100 \times 100$  receivers are evenly spaced along the surface ( $z = 0.0$  km) from  $(x, y) = (0.0, 0.0)$  km to  $(0.5, 0.5)$  km, with 5 m spacing in both x- and y-directions; the time sample increment is 0.5 ms. Each source is recorded by all receivers.

We use smoothed velocity and density models for ERTM, and apply the proposed 3D ERTM image condition. The migrated and stacked PP and PS images are shown in Figs. 4a and 4b. The PS image (Fig. 4b) has higher resolution and wider illumination than the PP image (Fig. 4a) because S-waves have shorter wavelengths and smaller reflection angles than the P-waves. The PP reflection angle in Fig. 4a is larger than the PS reflection angle in Fig. 4b. So the PS migrated images can get closer to the model edge,

and the horizontal shape of the PS illumination follows the rectangular shape of the receiver array. The PP horizontal illumination is smaller and more rounded than the PS because of its smaller incident angle aperture. Note that both the PP and PS images are single component [eq. (13)] and, because the PS image has consistent polarities across the source position, they will stack constructively, which is an essential advantage over using curl operators.

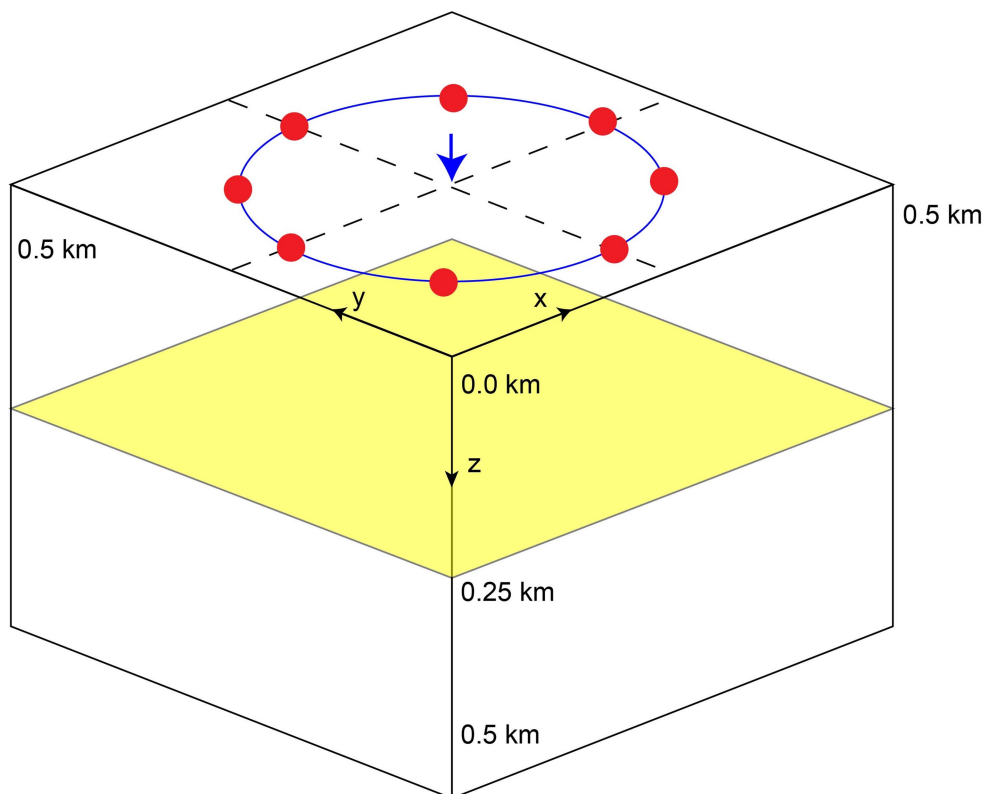


Fig. 3. Two-layer model; the red spots are eight sources, evenly placed on the surface along a circle with the center at  $(x, y) = (0.25, 0.25)$  km and radius = 0.02 km. The PP and PS ADCIGs are obtained beneath the surface position  $(0.25, 0.25)$  km as marked by the blue arrow.

We obtain PP and PS ADCIGs at the surface center  $(x, y) = (0.25, 0.25)$  km (also marked in Fig. 3 with the blue arrow). The data for each of the eight sources are migrated and the ADCIGs collapse to one point at the depth of the migrated image. The PP (Fig. 5a) and PS (Fig. 5b) ADCIG slices are shown in polar coordinates at the image depth (obtained by picking the maximum value within a depth window). The incident angles are indicated from the circle center ( $0^\circ$ ) to the outer circle ( $60^\circ$ ); the azimuth angles range from  $-180^\circ$  to  $+180^\circ$  (counterclockwise). The image positions on the polar plots (Fig. 5) indicate the incident and azimuth angles of the reflections. The images from the eight sources are easily identified on the polar plots as they have the same incident angles and different azimuth angles.

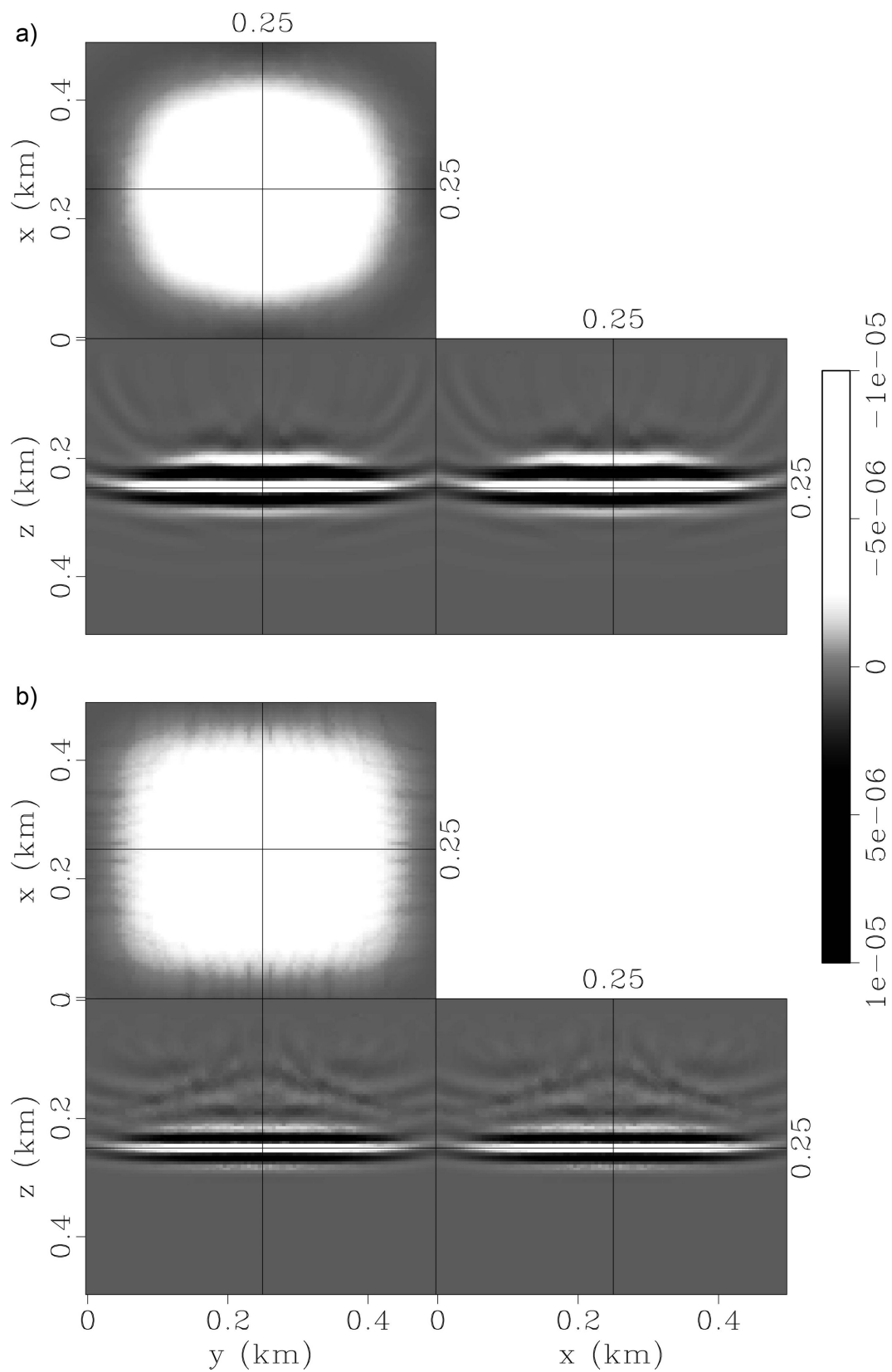


Fig. 4. (a) PP and PS stacked images obtained using 3D ERTM for eight sources using the vector image condition.

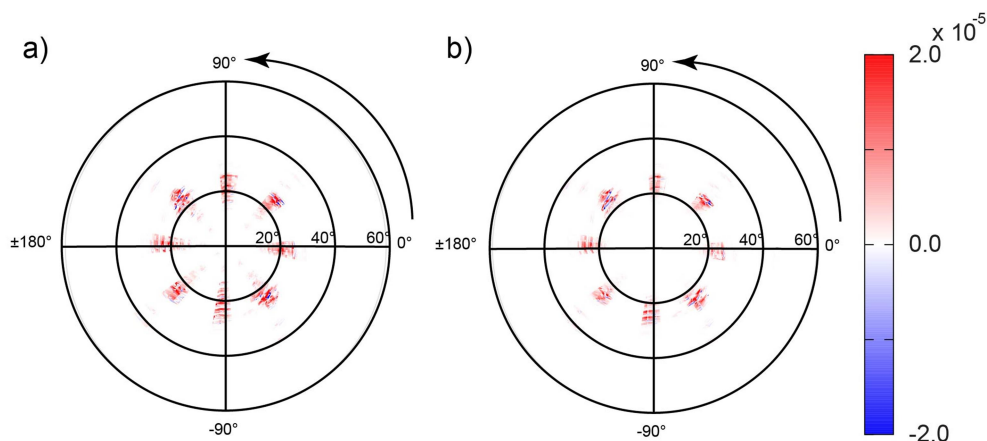


Fig. 5. (a) PP and (b) PS ADCIG slices in a polar coordinate system at surface position  $(0.25, 0.25)$  km (the maximum values within a depth window centered at  $z = 0.25$  km are plotted). Notice the eight sources can be identified on the ADCIGs as they have the same incident angles and different azimuth angles.

In the second test, we construct a 3D elastic example using the SEG/EAGE 3-D Overthrust model (<http://geodus1.ta.tudelft.nl/seage3dm/>), which is an acoustic model containing only the P-velocity ( $V_P$ ). To make the model elastic, we approximate  $V_S$  by dividing the  $V_P$  by 2 at each grid point. The density is set to be a constant  $2.4 \text{ g/cm}^3$ . Fig. 6a shows three orthogonal slices through the  $V_P$  volume containing the portion of the model used for this example; the size of this reduced volume (in grid points) is  $151 \times 151 \times 140$ , and the spatial interval of the model is  $dx = dy = dz = 25$  m. 256 sources are evenly placed in a square defined by  $x$  from 1.125 km to 2.625 km,  $y$  from 1.125 km to 2.652 km, and  $z = 0.025$  km. The sources are 15 Hz Ricker wavelets with 0.1 km intervals in both  $x$ - and  $y$ -directions.  $151 \times 151$  receivers are evenly placed over the surface with a spacing of 25 m. The direct waves in the generated seismograms are removed.

Two image conditions are used and compared in this test. In addition to the proposed image condition, a vector based dot-product image condition (Du et al., 2017) is also applied to provide benchmark results. The explicit forms and analytical comparisons between the two image conditions can be found in Appendix A. For both RTMs, we use the same smoothed velocity and density models (Fig. 6b). The migrated images using the dot-product image condition and the proposed image condition are shown in Figs. 7 and 8, respectively. Both images have (low amplitude) gaps where the steep dips and normal incidence coincide, as expected, because the steep dips are not well illuminated. Although both images are source normalized, the image amplitudes in Fig. 8 are stronger than in Fig. 7 because the proposed image condition allow wider incident angle information to be stacked (see the ADCIG comparisons below).

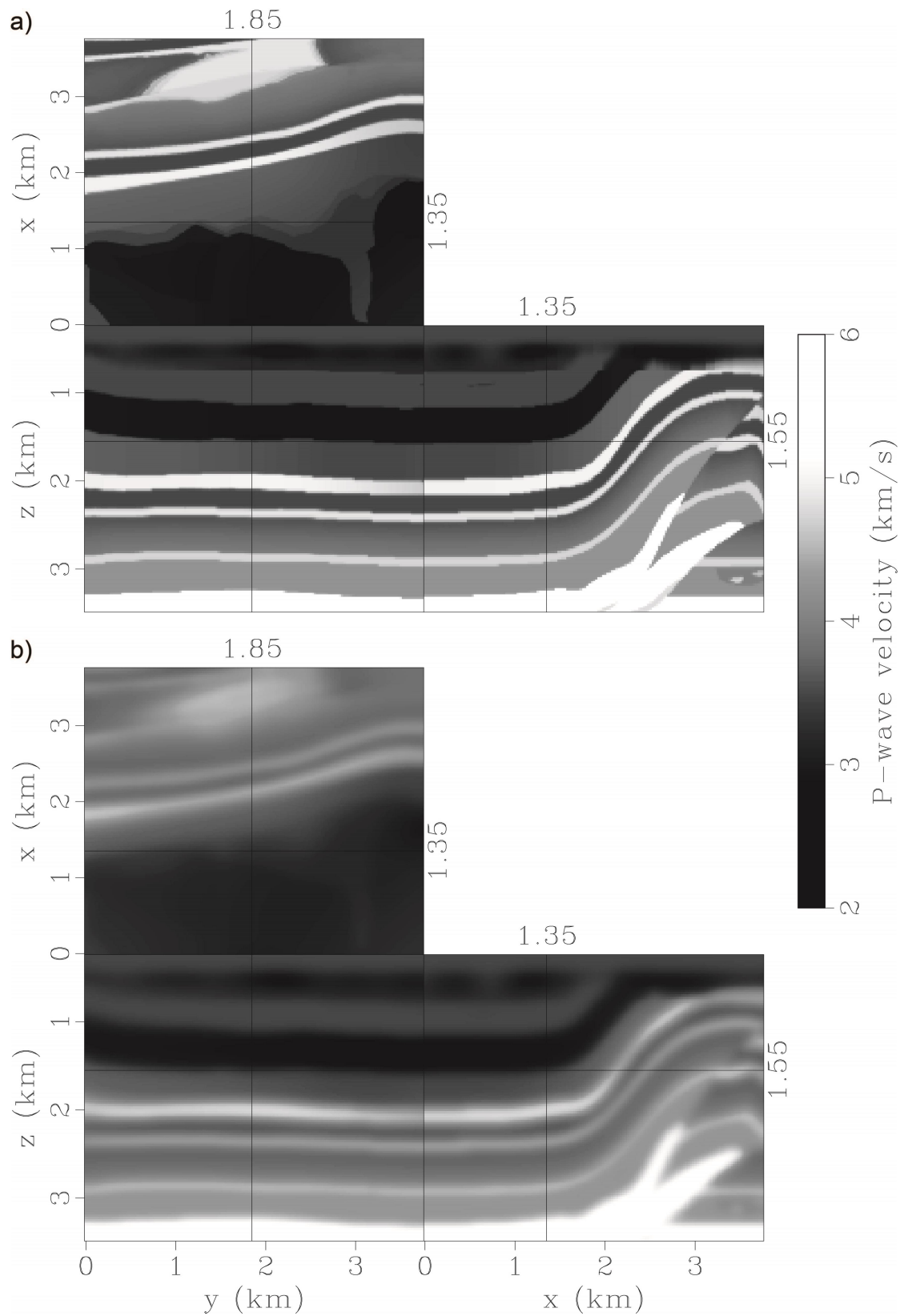


Fig. 6. (a) a portion of the Overthrust model (P-wave velocity) and (b) the smoothed model for ERTM.

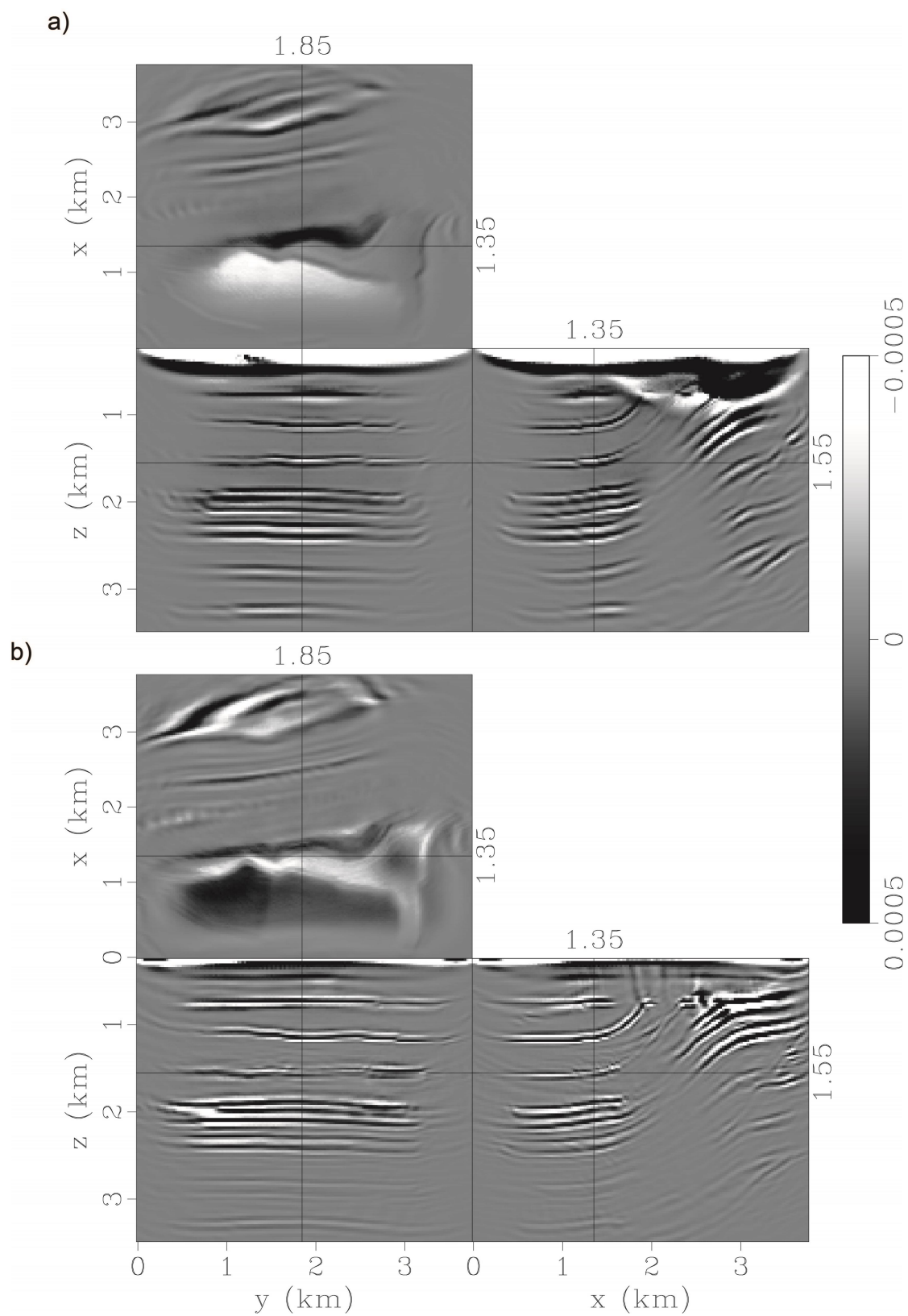


Fig. 7. Migrated (a) PP image and (b) PS image using the dot-product image condition.

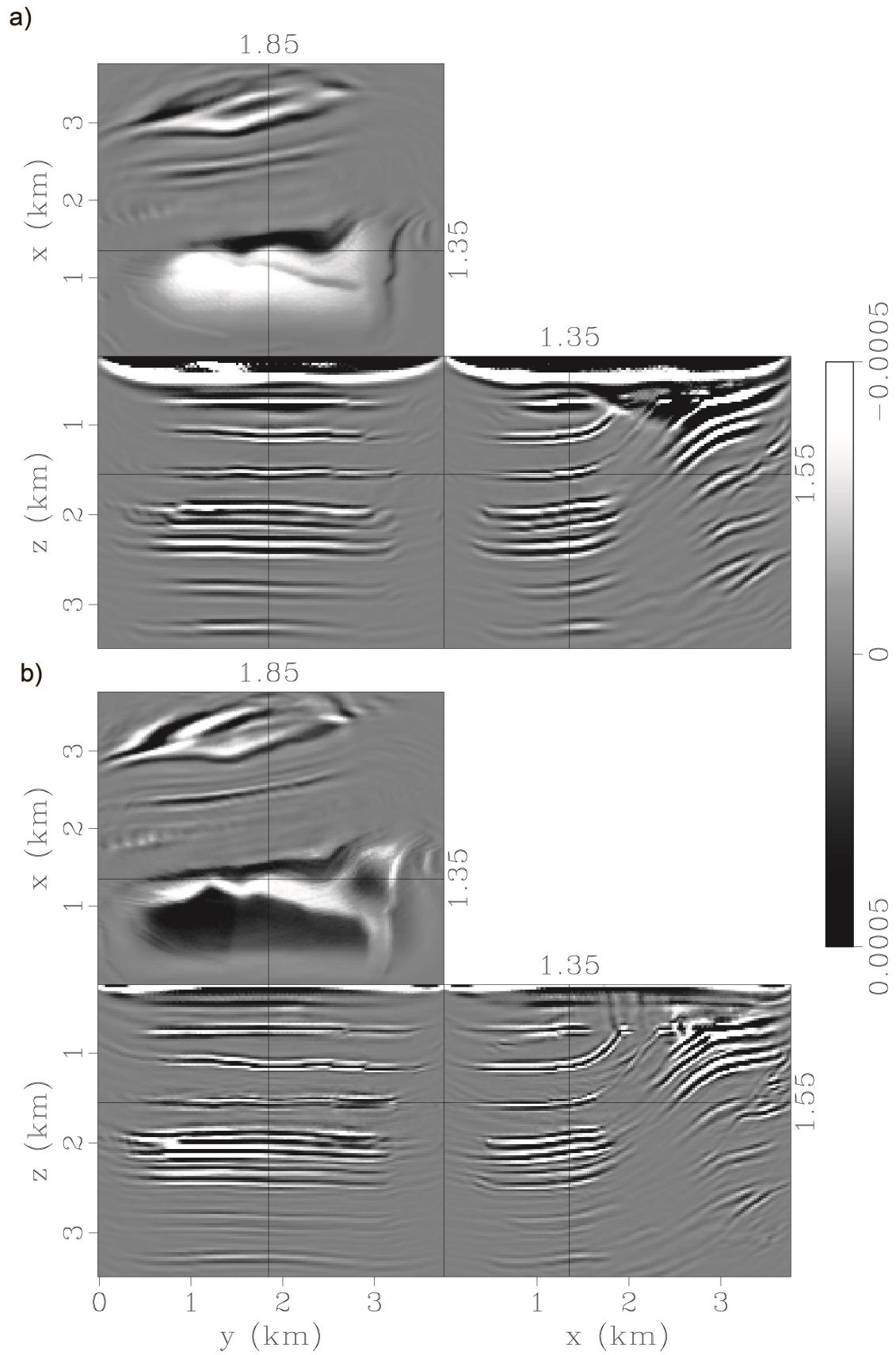


Fig. 8. Migrated (a) PP image and (b) PS image using the proposed image condition. The image amplitudes are stronger than those in Fig. 7.

Figs. 9 and 10 show the PP (upper row) and PS (lower row) ADCIGs using the dot-product and the proposed image conditions, respectively. Both sets of ADCIGs are extracted below the same surface location  $(x, y) = (1.35, 1.85)$  km. For viewing purposes, the azimuths of the ADCIGs are evenly binned into six bins from  $0^\circ$  to  $360^\circ$  around its surface position. Each bin contains the stacked ADCIGs over  $30^\circ$  of azimuth angle and their corresponding mirror azimuth, which are  $180^\circ$  apart from them (see the shaded area in the first row of Figs. 9 and 10).  $0^\circ$  azimuth corresponds to the positive x axis in Fig. 6, and  $90^\circ$  azimuth corresponds to the positive y axis. The incident angles are collected from  $0^\circ$  to  $50^\circ$ , and the signs of incident angles are determined relatively by their corresponding azimuth angles as indicated in Figs. 9 and 10. The events in the ADCIGs are flat over incident angles because smoothed velocity and density models are used for the ERTM. The migrated images from both image conditions (Figs. 7 and 8) and their corresponding ADCIGs (Figs. 9 and 10) have good correspondence to the geological structures in the model.

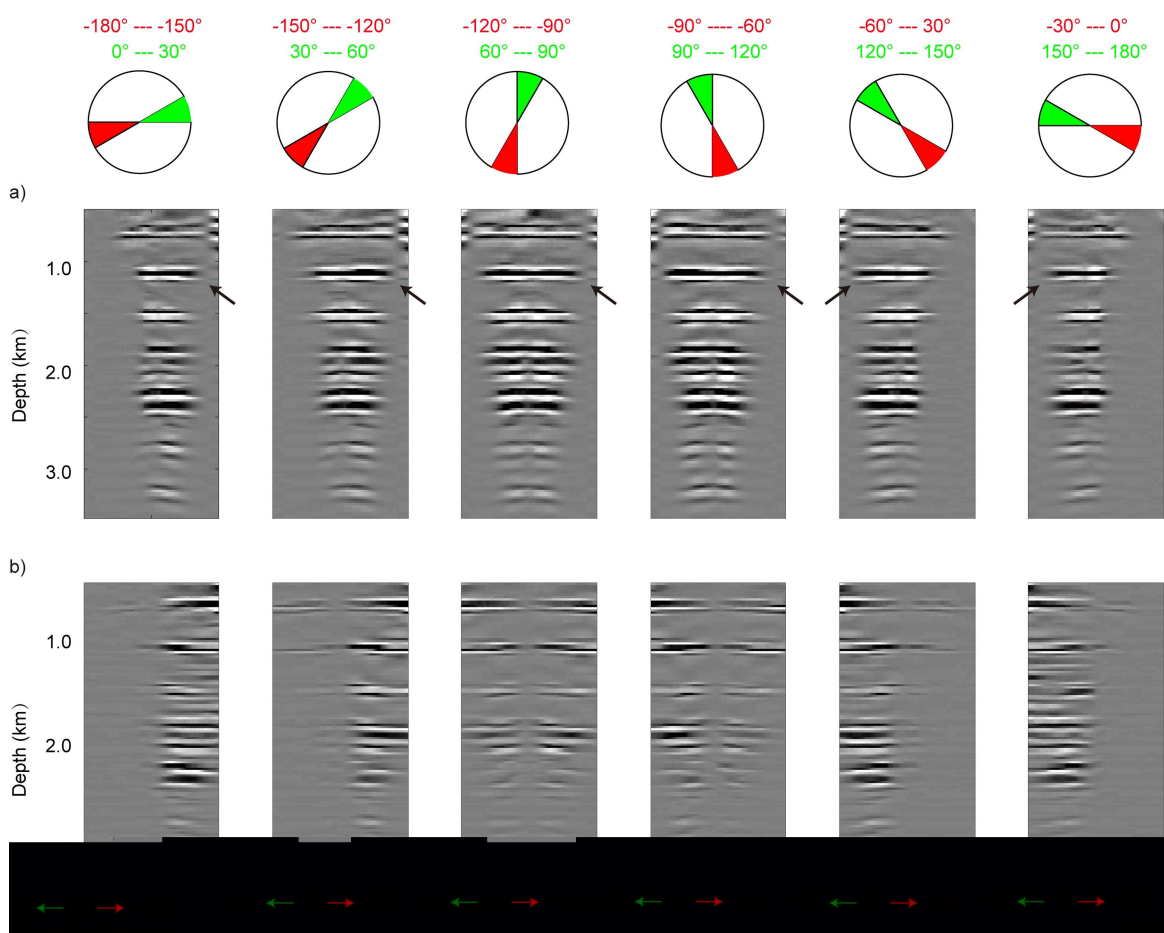


Fig. 9. (a) PP and (b) PS ADCIGs extracted at  $(x, y) = (1.35, 1.85)$  km plotted in six pie shaped azimuth angle bins from  $0^\circ$  to  $360^\circ$  in increments of  $30^\circ$ , using the dot-product image condition. Areas marked with arrows in the PP ADCIGs indicate the attenuation effect of  $\cos(\psi)$ ; compare with Fig. 10.

The amplitudes of the PP ADCIGs in the dot-product image condition diminish as the open angle approaches  $90^\circ$  (indicated by the black arrows in Fig. 9) because a multiplication of  $\cos(\psi)$  is implicit in the dot-product image condition, where  $\psi$  is the angle between the incident and reflected particle velocity vectors. For PP reflections,  $\cos(\psi)$  approaches 0 as the open angle  $2\theta$  approaches  $90^\circ$ . This problem is avoided using the proposed image condition (see the marked areas in Fig. 10), which replaces  $\cos(\psi)$  with a  $\text{sgn}$  (-1 or 1) function, and thus gives wider angle apertures than the former (see Appendix A for detailed analysis). The amplitudes in the PS ADCIGs are also changed, but do not diminish at  $2\theta = 90^\circ$  because the S-wave particle velocity vector is perpendicular to its propagation direction, and  $\psi$  is not the same as the open angle between the incident P- and converted S-waves.

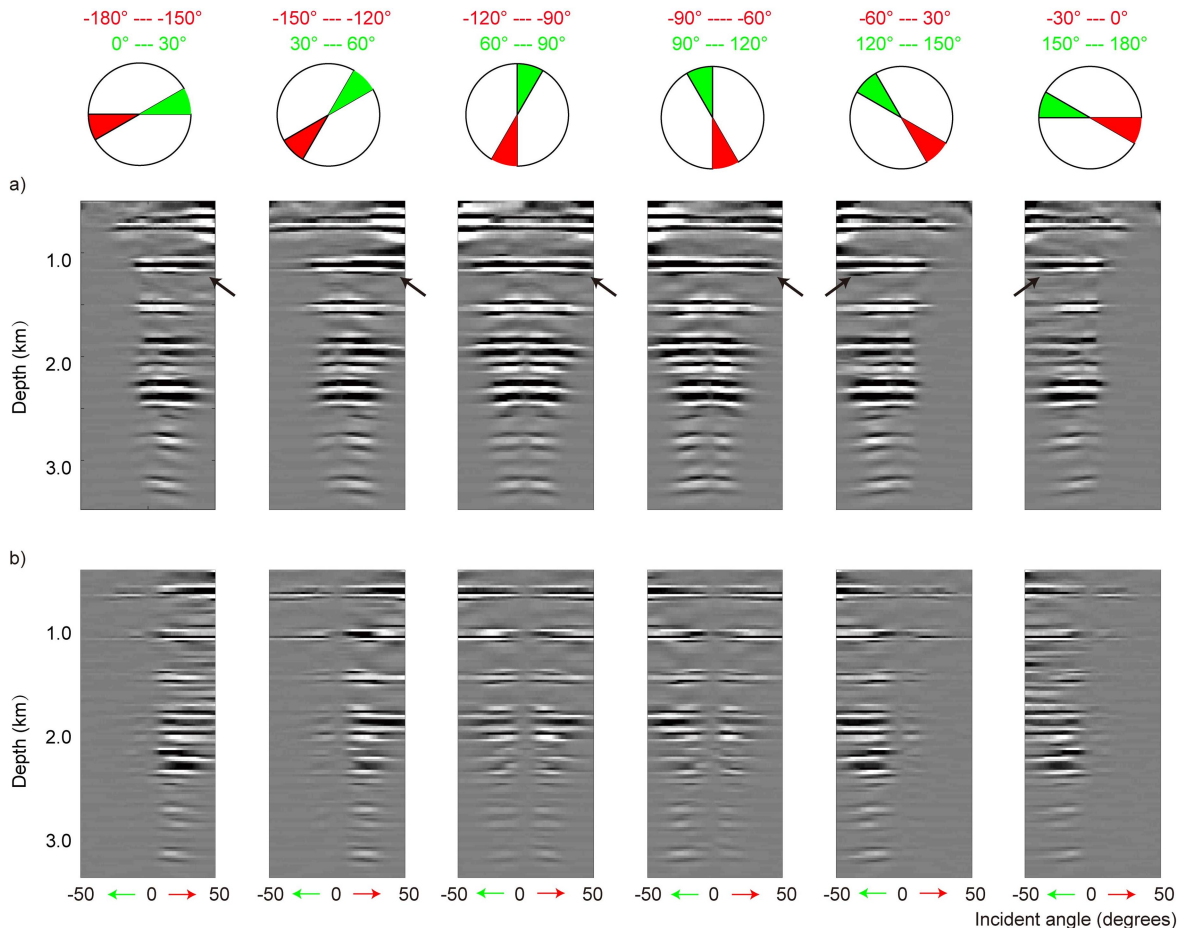


Fig. 10. (a) PP and (b) PS ADCIGs extracted at  $(x, y) = (1.35, 1.85)$  km plotted in six pie shaped azimuth angle bins from  $0^\circ$  to  $360^\circ$  in increments of  $30^\circ$ , using the proposed image condition. Compare the areas marked with arrows with those in Fig. 9; the proposed image condition generates PP ADCIGs with wider open angles than in the dot-product image condition, because the  $\cos(\psi)$  is not present in the proposed image condition.

## DISCUSSION

The proposed source-normalized magnitude-crosscorrelation elastic image conditions have several important differences from the source-normalized crosscorrelation image condition in acoustic RTMs (Kaelin and Guitton, 2006). First, the magnitudes of the elastic particle-velocity vectors are used instead of amplitudes in acoustic wavefields. Second, for acoustic RTMs, only a single  $\tau^p$  component amplitude needs to be stored during the source wavefield extrapolation, while in the proposed image condition for elastic RTM, all the P-wave particle-velocity and stress components are required at each grid point to build the final image. Third, because the magnitudes of the particle-velocity vectors are always positive, to get accurate reflectivity information, signs of the reflections (both PP and PS) need to be determined as a part of the image condition. The output of the ERTM contains approximate angle-dependent reflectivity information; to increase the accuracy of the reflectivity, compensations for transmission and attenuation losses (Deng and McMechan, 2007, 2008) are also necessary.

In the above examples, we store the source wavefield in disk as the models are small. However, for big 3D models, the wavefield storage and I/O burden may become costly. One solution is to store the boundaries or checkpoints during the source wavefield extrapolation (Nguyen and McMechan, 2015), and to reconstruct the source wavefield during the receiver wavefield extrapolation.

The accuracy of Poynting vectors decreases as the model becomes complicated and wavefronts interfere with each other. Common solutions include increased smoothing of the velocity model, and precalculating the dip angles of the subsurface structures to provide additional information in constructing ADCIGs (Zhang and McMechan, 2011). Some gaps at near-normal incident angles which are caused by ambiguities in the azimuth angle calculations, may appear in the PP ADCIGs. We use linear interpolation to fill the gaps for better viewing in Figs. 9 and 10.

Compared with the excitation amplitude type image condition (Wang and McMechan, 2015, 2016), the crosscorrelation type image condition involves substantially more wavefield storage and a large I/O burden, and thus is more computationally expensive; the main benefit is that multipathing can be handled efficiently and correctly.

The proposed image condition uses the relation between P- and S-wave directions and their corresponding polarization directions, which is valid in isotropic media. In anisotropic media, the relation is more complicated (Wang et al., 2016a), and an extension of this image condition to anisotropic ERTM needs further investigations.

## CONCLUSIONS

A source-normalized magnitude-crosscorrelation image condition using signed magnitudes of elastic components is proposed and implemented in 3D ERTMs. P- and S-waves are decomposed in the vector domain during both source and receiver wavefield extrapolation. Propagation directions for P- and S-waves are efficiently calculated using Poynting vectors with the decomposed P- and S-wave vectors as input, and make the process of generating ADCIGs much cheaper compared with other existing methods that involve extracting propagation directions from wavefronts. Comparisons with an existing vector-based dot-product image condition show PP ADCIGs with wider incident angles than the existing dot-product elastic image condition.

## ACKNOWLEDGEMENTS

The research leading to this paper is supported by the National Natural Science Foundation of China under grant number NSFC 41804108, by the Fundamental Research Funds for the Central Universities under grant number 01113026, and by the Sponsors of the UT-Dallas Geophysical Consortium. A portion of the computations were done at the Texas Advanced Computing Center. This paper is Contribution No. 1334 from the Department of Geosciences at the University of Texas at Dallas.

## REFERENCES

- Aki, K. and Richards, P.G., 1980. *Quantitative Seismology, Theory and Methods*. W.H. Freeman and Co., Sausalito.
- Aminzadeh, F., Burkhard, N., Nicoletis, L., Rocca, F. and Wyatt, K., 1994. SEG/EAGE 3-D modeling project: 2nd update. *The Leading Edge*, 13: 949-952.
- Červený, V., 2001. *Seismic Ray Theory*. Cambridge University Press, Cambridge.
- Chang, W. and McMechan, G.A., 1986. Reverse-time migration of offset vertical seismic profiling data using the excitation-time imaging condition. *Geophysics*, 51: 67-84.
- Chang, W. and McMechan, G.A., 1994. 3-D elastic prestack reverse-time depth migration. *Geophysics*, 59: 597-609.
- Cheng, J. and Fomel, S., 2014. Fast algorithms for elastic-wave-mode separation and vector decomposition using low-rank approximation for anisotropic media. *Geophysics*, 79(4): C97-C110.
- Claerbout, J., 1985. *Imaging the Earth's Interior*. Blackwell Scientific Publications Inc., New York.
- Dai, F.T. and Kuo, J.T., 1986. Real data results of Kirchhoff elastic wave migration. *Geophysics*, 51: 1006-1011.
- Deng, F. and McMechan, G.A., 2007. True-amplitude prestack depth migration. *Geophysics*, 72(3): S155-S166.
- Deng, F. and McMechan, G.A., 2008. Viscoelastic true-amplitude prestack reverse-time depth migration. *Geophysics*, 73(4): S143-S155.
- Du, Q., Going, X., Zhu, Y., and Fang, G., 2012. 3D PS-wave imaging with elastic reverse time migration. *Geophysics*, 79(5): S173-S184.

- Du, Q., Gong, X., Zhang, M., Zhu, Y. and Fang, G., 2014. 3D PS-wave imaging with elastic reverse-time migration. *Geophysics*, 79(5): S173-S184.
- Du, Q., Guo, C., Zhao, Q., Gong, X., Wang, C. and Li, X., 2017. Vector-based elastic reverse time migration based on scalar imaging condition. *Geophysics*, 82(2): S111-S127.
- Gray, S.H., Etgen, J., Dellinger, J. and Whitmore, D., 2001. Seismic migration problems and solutions. *Geophysics*, 66: 1622-1640.
- Hokstad, K., 2000. Multicomponent Kirchhoff migration. *Geophysics*, 65: 861-873.
- Jin, H. and McMechan, G.A. and Guan, H., 2014. Comparison of methods for extracting ADCIGs from RTM. *Geophysics*, 79(3): S89-S103.
- Jin, H., McMechan, G.A. and Nguyen, B.D., 2015. Improving I/O performance in 2D and 3D ADCIGs from RTM. *Geophysics*, 80(2): S65-S77.
- Kaelin, B. and Guitton, A., 2006. Imaging condition for reverse time migration. Expanded Abstr., 76th Ann. Internat. SEG Mtg., New Orleans: 2594-2598.
- Komatitsch, D. and Martin, R., 2007. An unsplit convolutional perfectly matched layer improved at grazing incidence for the seismic wave equation. *Geophysics*, 72(5): SM155-SM167.
- Kuo, J.T. and Dai, F.T., 1984. Kirchhoff elastic wave migration for the case of noncoincident source and receiver. *Geophysics*, 49: 1223-1238.
- Ma, D. and Zhu, G., 2003. P- and S-wave separated elastic wave equation numerical modeling (in Chinese). *Oil Geophys. Prosp.*, 38(5): 482-486.
- Madariaga, R., 1976. Dynamics of an expanding circular fault. *Bull. Seismol. Soc. Am.*, 66: 639-666.
- Nguyen, B.D. and McMechan, G.A., 2013. Excitation amplitude imaging condition for prestack reverse-time migration. *Geophysics*, 78(1): S37-S46.
- Nguyen, B.D. and McMechan, G.A., 2015. Five ways to avoid storing source wavefield snapshots in 2D elastic prestack reverse-time migration. *Geophysics*, 80(1): S1-S18.
- Rocha, D., Tanushev, N. and Sava, P., 2016. Isotropic elastic wavefield imaging using the energy norm. *Geophysics*, 81(4): S207-S219.
- Shabelansky, A.H., Malcolm, A. and Fehler, M., 2017. Converted-wave seismic imaging: Amplitude-balancing source-independent imaging conditions. *Geophysics*, 82(2): S99-S109.
- Sheriff, R.E. and Geldart, L.P., 1995. *Exploration Seismology*, 2nd Ed. Cambridge University Press, Cambridge.
- Stewart, R.R., 2001. Joint P and P-SV inversion. Technical Report. CREWES Research Report.
- Sun, R. and McMechan, G.A., 2001. Scalar reverse-time depth migration of prestack elastic seismic data. *Geophysics*, 66(5): 1518-1527.
- Virieux, J., 1984. SH-wave propagation in heterogeneous media: Velocity-stress finite-difference method. *Geophysics*, 49: 1933-1957.
- Virieux, J., 1986. P-SV wave propagation in heterogeneous media: Velocity-stress finite-difference method. *Geophysics*, 51: 889-901.
- Wang, C., Cheng, J. and Arntsen, B., 2016. Scalar and vector imaging based on wave mode decoupling for elastic reverse time migration in isotropic and transversely isotropic media. *Geophysics*, 81(5): S383-S398.
- Wang, W., Hua, B., McMechan, G.A. and Duquet, B., 2018. P and S decomposition in anisotropic media with localized low-rank approximations. *Geophysics*, 83(1): C13-C26.
- Wang, W. and McMechan, G.A., 2015. Vector-based elastic reverse-time migration. *Geophysics*, 80(6): S245-S258.
- Wang, W. and McMechan, G.A., 2016. Vector-based image condition for 3D elastic reverse time migrations. Expanded Abstr., 86th Ann. Internat. SEG Mtg., Dallas: 4168-4172.
- Wang, W., McMechan, G.A., Tang, C. and Xie, F., 2016. Up/down and P/S-decompositions of elastic wavefields using complex seismic traces with applications to calculating Poynting vectors and angle-domain common-image gathers from reverse time migrations. *Geophysics*, 81(4), S181-S194.

- Wang, W., McMechan, G.A. and Zhang, Q., 2015. Comparison of two algorithms for isotropic elastic P and S vector decomposition. *Geophysics*, 80(4): T147-T160.
- Wapenaar, C.P.A. and Haimé, G.C., 1990. Elastic extrapolation of primary seismic P- and S-waves. *Geophys. Prosp.*, 38: 23-60.
- Whitmore, N.D., 1995. An imaging hierarchy for common-angle seismograms. Ph.D. Thesis, University of Tulsa, Tulsa.
- Xiao, X. and Leaney, W.S., 2010. Local vertical seismic profiling (VSP) elastic reverse-time migration and migration resolution: Salt-flank imaging with transmitted P-to-S waves. *Geophysics*, 75(2): S35-S49.
- Yan, J. and Sava, P., 2008. Isotropic angle-domain elastic reverse-time migration. *Geophysics*, 73(6): S229-S239.
- Zhang, J., Tian, Z. and Wang, C., 2007. P- and S-wave separated elastic wave equation numerical modeling using 2D staggered-grid. *Expanded Abstr.*, 77th Ann. Internat. SEG Mtg., San Antonio: 2104-2109.
- Zhang, Q. and McMechan, G.A., 2011. Direct vector-field method to obtain angle-domain common-image gathers from isotropic acoustic and elastic reverse time migration. *Geophysics*, 76(5): WB135-WB149.
- Zhu, H., 2017. Elastic wavefield separation based on the Helmholtz decomposition. *Geophysics*, 82(2): S173-S183.

## APPENDIX A

### RELATIONS AND DIFFERENCES BETWEEN THE PROPOSED AND THE DOT-PRODUCT IMAGE CONDITIONS

Both the proposed image condition and the vector dot product image condition (Wang et al., 2016a; Zhu, 2017; Du et al., 2017) involve projections from vector wavefields to scalar images; the latter image condition applies a dot product, whereas our image condition calculates the signed magnitudes from the wavefields.

To make the comparison vivid, we modify the proposed image condition (13), which is a source-normalized crosscorrelation image condition, to be a crosscorrelation type image condition without source normalization as follows

$$I_{pp}(x, y, z) = \sum_{t=0}^T \text{sgn}_{pp}(x, y, z, t) |\mathbf{V}_{rec}^p(x, y, z, t)| |\mathbf{V}_{src}^p(x, y, z, t)|, \quad (\text{A-1})$$

and

$$I_{ps}(x, y, z) = \sum_{t=0}^T \text{sgn}_{ps}(x, y, z, t) |\mathbf{V}_{rec}^s(x, y, z, t)| |\mathbf{V}_{src}^p(x, y, z, t)|. \quad (\text{A-2})$$

The non-normalized dot product image conditions can be written as

$$I_{pp}(x, y, z) = \sum_{t=0}^T \mathbf{V}_{rec}^p(x, y, z, t) \cdot \mathbf{V}_{src}^p(x, y, z, t), \quad (\text{A-3})$$

and

$$I_{ps}(x, y, z) = \sum_{t=0}^T \mathbf{V}_{rec}^s(x, y, z, t) \cdot \mathbf{V}_{src}^p(x, y, z, t), \quad (\text{A-4})$$

where  $\mathbf{V}_{rec}$  and  $\mathbf{V}_{src}$  are the decomposed (P or S) receiver and source vector wavefields. Recall that

$$\mathbf{V}_{rec} \cdot \mathbf{V}_{src} = |\mathbf{V}_{rec}| \cdot |\mathbf{V}_{src}| \cos(\psi), \quad (\text{A-5})$$

where  $\psi$  is the angle between the incident and reflected particle velocity vectors, and the  $\cos(\psi)$  causes an image amplitude change which is not related to the subsurface properties.

A solution proposed by Du et al. (2017) is to correct the image amplitudes by dividing the  $I_{pp}$  and  $I_{ps}$  by  $[\cos(\psi) + \varepsilon^2]$  [eq. (13) in Du et al. (2017)] where  $\varepsilon^2$  is a small number that prevents division by zero. This correction is valid if the calculation of  $\psi$  is robust and accurate, but the correction accuracy decreases as  $\psi$  approaches  $90^\circ$ .

There is no need for amplitude correction in the proposed image condition, and  $\psi$  doesn't need to be accurate as it is only used for sign determination. The only difference between image conditions (A-1) and (A-2) and image conditions (A-3) and (A-4), is that  $\cos(\psi)$  is replaced by a sgn function in (A-1) and (A-2) that is pre-calculated in eqs. (12).